Author: Vlieg, R.C.
Title: Two-photon multifocal microscopy for in vivo single-molecule and single-particle imaging
Issue Date: 2020-12-14

Chapter 4

Wide-field two-photon imaging of single fluorophores by structured illumination

Single molecule microscopy is often hampered by autofluorescence and *in vivo* inelastic scattering impairs the visibility of the weak signal from single fluorophores. Two-photon microscopy decreases background fluorescence by using near-infrared light, and reduces the excitation volume due to the non-linear excitation mechanism, and limits out-of-focus photodamage and bleaching. However, the low two-photon absorption cross-section of most fluorophores requires a high light intensity. This is usually implemented by confocal scanning and yields lower frame rates and increases photobleaching. Here we build on previous efforts using multifocal excitation to increase the image speed, and compare two scanning modes that both yield a wide field light-sheet-like excitation. In live zebrafish embryos background fluorescence and photobleaching are further reduced, enabling tracking of single fluorophores for more than 30 seconds. Furthermore, we show that multifocal excitation with structured light sheet illumination suppresses background in highly scattering environments. Finally, we used single-molecule tracking to quantify diffusive behavior of single eGFP-HRas molecules and observed longer and less confined tracks, that suggest that the mobility of these proteins differs in different regions of the same cell. The experiments demonstrate for the first time that two-photon microscopy can readily be used for *in vivo* single-molecule tracking and, contrary to previous reports, it is shown to reduce photobleaching, while achieving significantly improved signal to noise ratios.

Contributing authors:
Vlieg, R. C., Gora, R., Pham, C., Schaaf, M., van Noort, J.

4.1 INTRODUCTION

Single molecule fluorescence microscopy has been fundamental for quantitative understanding on how biological systems function at the microscale. The ability to track a protein in space and time allows to study behavior normally obscured by the ensemble of molecules. To resolve the weak signal from a single fluorophore, often residing within a complex and scattering environment, efficient signal collection and background suppression is required. Total internal reflection microscopy (TIRF) reduces background signal by illuminating only in near-field, limiting the detection of fluorophores to within ±100 nm from the cover glass[1]. For three-dimensional (3D) tracking of fluorophores a larger volume needs to be illuminated, which generally necessitates a pinhole to reject out-of-focus light, as done in fluorescence correlation spectroscopy (FCS)[2], laser scanning confocal[3], and spinning-disc microscopy[4]. Although effective for reducing background, fluorophores that do not contribute to the image still suffers from photobleaching outside the focal volume.

A more preferable scenario for tracking fluorophores in 3D would be to excite only within the focal volume, thereby eliminating out-of-focus signal. Two-photon microscopy (TPM) does exactly this by confining excitation to a volume defined by a quadratic dependence on laser power[5]. Moreover, excitation by near-infrared light allows for deeper imaging into tissues[6] and reduces autofluorescence[7]. Despite these advantages single fluorophore studies with TPM have been limited mostly to *in vitro* experiments[8–16].

One major issue with two-photon excitation (TPE) is fluorophore stability. The high photon intensity in the focal volume and the promotion of a fluorophore to higher order excited states result in bleaching times that are typically a factor 3 – 5 shorter compared to single-photon excitation[10,17,18]. Also, the low two-photon absorption cross section ($\sigma^{(2)}$) of most commonly used fluorophores diminishes fluorophore brightness, necessitating longer pixel dwell times or even higher laser power. Unfortunately, bleaching scales with laser power to an exponential power larger than 2, while fluorescence scales only quadratically[14,17,19–21]. This prevents capturing single fluorophores at a high temporal and spatial resolution for extended periods of time. For example, using quasi wide-field TPE, proteins tagged by a single fluorophore were tracked on an artificial cellular membrane[13]. Although the reported background of the membrane was drastically reduced from 400 counts pixel^{-1} ms^{-1} with one-photon, to 3.4 counts pixel^{-1} ms^{-1} with TPE, most fluorophores lost their fluorescence before 20 images could be taken.

The issue of photobleaching by TPE calls for an illumination method where laser power is reduced, while tracking applications require pixel acquisition rates that are sufficiently high to capture single fluorophores over a large field-of-view (FOV). To achieve a N-fold increase in pixel rate at the same signal-to-noise ratio (SNR), a two-photon single-focus microscope (TPSM) would need $\sqrt{N}$ higher laser intensity. Two-photon multifocal microscopy (TPMM) improves acquisition speeds by *N* by splitting the excitation beam into *N* beamlets[22]. Unlike TPSM, the increase in speed is achieved without increasing the excitation power in each focus. This property suggests that higher frame rates can be achieved with TPMM at similar bleach rates as TPSM, or that bleaching times can be extended when imaging a similar-sized FOV. TPMM can be readily implemented by using passive optical elements to split the laser beam (e.g. diffractive optical elements (DOEs)[23,24], beam splitters[25,26]) and a camera to detect emission from the multiple foci.

A drawback of TPMM is the increase in background signal from scattered emission photons reaching incorrect camera pixels. Especially for highly scattering biological samples, low background signal is essential to resolve the weak signals of single fluorophores. A number of methods have been developed to suppress background from diffused emission light. In a de-scanned approach, the position of the emission beamlets remains stationary irrespective of the scanner motion by reflecting the emission photons back along the scanning mirror onto a multi-anode photomultiplier tube. This allows to collect more scattered photons onto the right detector and achieving higher contrast at deeper imaging depths[27,28]. Improvements were made in SNR by reducing the emission path-length in a non-descanned approach and increasing the distance between each focus[29]. Still, the low quantum efficiency (±16%) of multianode photomultipliers and the limited imaging speeds gain impairs detection of single fluorophores. By using a Richardson-Lucy deconvolution method to correct the location of the scattered photons, no additional optics is needed for background suppression while employing a sCMOS camera with a high quantum efficiency (82%)[24]. Structured illumination microscopy (SIM) has similar benefits to deconvolution. SIM suppresses background by filtering out the low spatial frequency noise from the image signal, resulting in enhanced contrast[30–32].

Here we combine structured illumination with TPE into structured light sheet illumination microscopy (SLIM). Besides changing the scan-pattern and the image reconstruction, SLIM requires no additional optics compared to conventional TPMM. SLIM uses multiple frequency-modulated images to compute a reconstructed image. In subsequent images, illumination patterns are spatially shifted and the total set of images illuminate the full FOV. By applying a discrete Fourier transform to the stack of images, all signal with frequencies other than the modulation frequency are suppressed – thus reducing background. SLIM is compatible with high-quantum efficiency camera detectors which are required for single molecule detection[33].

In this work we explore the TPMM capability of imaging single fluorophores in wide-field. Dividing excitation power over multiple foci resulted in 5-fold higher acquisition speeds at similar bleaching rates compared to confocal TPM. We also investigated the ability of SLIM to further reduce the background intensity in zebrafish embryos (*Danio rerio*) and compare the result to previously established spiral-scanning illumination[34]. Using SLIM, background signal was reduced to below single-molecule brightness in the highly scattering zebrafish embryos environments. Subsequent measurements revealed individual eGFP tagged HRas proteins as they moved across the membrane. The limited *in vivo* photobleaching allowed us to track molecules for hundreds of frames. The ability to measure single fluorophores for extended periods of time enables the study of protein dynamics normally obscured by photobleaching in more established microscopy techniques like total internal reflection fluorescence (TIRF) microscopy. These properties make TPMM combined with SLIM a new and promising technique for single molecule studies.

4.2 MATERIALS AND METHODS

Microscopy setup. A tunable near-IR Ti:Sa laser (Coherent, Chameleon Ultra) was coupled into a home-build two-photon multifocal microscope. A diffractive optical element (DOE, custom made by Holo-eye) diffracted the laser beam into an array of 10 x 10 beamlets. A fast-scanning mirror (FSM, Newport, FSM-300-1) scanned the beamlets across the excitation plane. The laser beams were focused using 60X NA 1.49 oil objective (Nikon, CFI60 Apochromat TIRF 60XC) mounted on a piezo-stage (PI, P-726 PIFOC), illuminating an area of 40 µm x 40 µm. Two-photon luminescence was collected by the same objective, filtered with a dichroic mirror (Semrock, 700dcxr) and two short pass filters (Semrock, FF01-720-SP & FF01-750-SP) and focused on a 2048 x 2048 pixel back-illuminated sCMOS camera (Photometrics, Prime BSI). Additional band pass filters, mounted in a motorized fast-change filter wheel (Thorlabs, FW103H/M), were positioned in front of the camera. Using self-written LabVIEW (National Instruments) software, the scanning mirror, focusing stepper motors and camera were controlled synchronously. For imaging of the zebrafish embryo the objective was replaced by a 25X NA 1.1 water objective (Nikon, CFI75 Apochromat 25XC) and the DOE was replaced by another DOE that generated a pattern of 25 x 25 beamlets (custom made by Holo-eye). This yielded an illuminated area of 180 µm x 180 µm.

Spiral illumination. For spiral scanning, the FSM was driven by an Archimedean spiral to rapidly scan the beams producing a fairly homogeneous illuminated wide-field, as characterized before[34]. A single period of the spiral scan took 200 ms and was synchronized with the camera integration time.

SLIM. For structured illumination the beamlets were scanned in four periods of a sinusoidal pattern in one direction (y). The amplitude in y-direction was 3 times the distance between neighboring foci (d), with d = 7.5 µm. The relative large amplitude resulted in more regular illumination than when the amplitude matched the spot-to-spot distance, especially at the maxima and minima of the periodic sweep. Four oscillations of the scanning beam were synchronized with integration time for one frame, which resulted in a “phase image” (g_n), as shown in Figure 4.1. Next, the beamlets were translated in x direction by $(d - \omega)/N$, with ω the full-width at half maximum of the point spread function of the system (0.39 µm) and *N* the number of phase images per SLIM image. With *d*/2 = 3.25 µm, the optimal *N* was given by d/ω_{PSF} = 8.3, which was rounded down to spatially sample the entire field-of-view (FOV). Between successive images there was a dead time of 5 ms, plus 1 ms per 128 pixel lines, which was used to empty the camera buffer into solid state storage and to reposition the FSM. The brief pauses between acquisition resulted in a total exposure duty cycle of 0.96. SLIM images were reconstructed via:

$$I\,(x,y) = \left|\sum_{n=1}^{N} g_n(x,y)e^{-i\varphi_n}\right| \tag{4.1}$$

with the spatial phase φ_n defined as:

$$\varphi_n = \frac{2\pi(n-1)}{n} \tag{4.2}$$

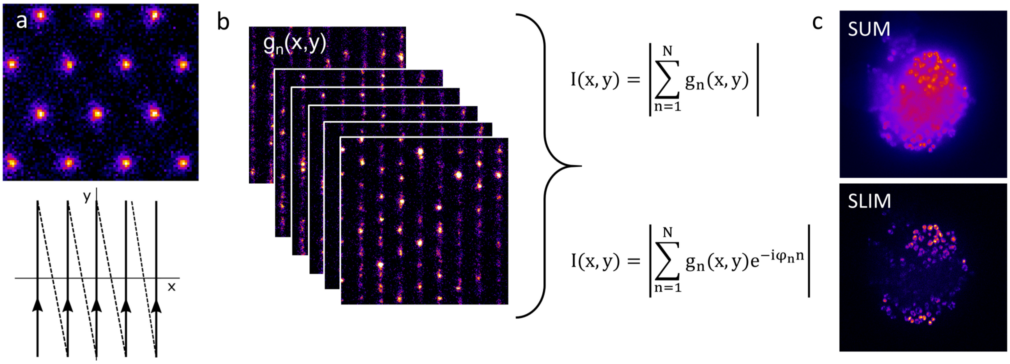

Figure 4.1: SLIM reconstruction reduces background signal. (a) To create a single SLIM image, the foci-pattern is linearly scanned across the image plane with a small lateral shift in each image. (b) *n* phase-images (g_n) are combined to yield either a conventional image, or a frequency selected reconstructed image, by a discrete Fourier transformation. (c) The summated image of a spheroid cluster of cells features a high intensity with a maximum at the center of the spheroid. In the SLIM image, reduction of scattered photons makes single cells clearly visible.

Rhodamine 6G sample preparation. Glass coverslips were sonicated in ethanol for 30 minutes, dried in a stream of nitrogen and treated in a UV-cleaner for 30 minutes. After cleaning, 100 µl of rhodamine 6G solution [100 pg/µl] (Sigma-Aldrich, 83697) was pipetted onto the glass surface and gently removed after 3 minutes under a nitrogen stream.

For the bleaching experiments the concentration of rhodamine 6G was increased to 100 ng/µl to form a homogenous layer on the glass surface.

Rhodamine-labeled DNA. Rhodamine-5-dUTP (11534378910, Sigma-Aldrich) was enzymatically incorporated into DNA using polymerase chain reaction (PCR). Plasmid pUC18 DNA was used as a template. A 100 µl PCR mixture contained 2.5 units of FastStart Taq DNA polymerase (5U/µl), 10 µM of forward (5' CTC CAA GCT GGG CTG TGT 3') and 10 µM backward primers (5' GAT AAA TCT GGA GCC GGT GA 3'), 100µM of dNTPs and 50 µM of rhodamine-5-dUTP and 1X PCR reaction buffer with 10X $MgCl_2$. The PCR reaction was run with the following program: step 1: 240 seconds at 95 ºC; step 2: 30 seconds at 95 ºC; step 3: 30 seconds at 49 ºC; step 4: 45 seconds at 72 ºC; step 5: 300 seconds at 72 ºC. Steps 2-4 were cycled 40 times. The PCR products were purified with a Promega Wizard SV Gel & PCR cleanup kit following the manufacturers' protocol. The concentration of the DNA substrate was measured with UV/Vis spectrophotometer (BioDrop µLITE, Isogen Life Science).

Flowcell preparation. The DNA-rhodamine constructs were immobilized inside flow cells. Glass coverslips were sonicated for 30 minutes in ethanol and UV-cleaned for an additional 30 minutes. After cleaning, flow cells were constructed by sandwiching double-sided stickers between the cover slips. Rectangular holes were cut into the stickers to create channels of approximately 50 µl per channel. The flow cell was mounted onto a laser cut scaffold for stability and to facilitate for pipetting solutions into the channel. Once constructed, the channels were incubated with a 0.01% (w/v) poly-L-lysine solution (P4707, Sigma-Aldrich) for 30 minutes. After gently flushing with 150 µl HPLC-grade water, 50 µl of 100 pM DNA was injected and incubated for 3 minutes. After 3 minutes the flow cell was again gently flushed with 150 µl of HLPC-grade water and ready for imaging.

Zebrafish embryos. Zebrafish (*Danio rerio*, strain AB/TL) were maintained and handled according to the guidelines from the Zebrafish Model Organism Database (http://zfin.org) and in compliance with the directives of the local animal welfare committee of Leiden University. Fertilization was performed by natural spawning at the beginning of the light period, and eggs were raised at 28.5 °C in egg water (60 µg/ mL Instant Ocean sea salts). The previously established *Tg(kdrl:mTurquoise)* zebrafish line was used yielding fluorescence in the endothelial cells by fusion of the fluorescent protein mTurquoise to the vascular endothelial growth factor *kdrl*[35]. Three-day post fertilization (*dpf*) old embryos were anesthetized in 0.01% tricaine and placed onto a glass coverslip. Embedding the embryos in 0.4% agarose before imaging minimized movement. For the single molecule measurements, transfection of eGFP-C10H-Ras into *kdrl* line embryos and sample mounting was done according to previously described protocol[36]. In short, zebrafish eggs at the one- to two cell stage were microinjected with eGFP-C10H-Ras mRNA (30pg/egg). At three *dpf*, embryos were positioned on their side on a glass coverslip and a ±0.75 mm thick sheet of agarose was placed over the tail section of the embryo for imaging.

Simulations. Simulations of single molecule measurements by spiral illumination and SLIM were done in Pyhton 3 code. A pattern of foci was generated based on the actual distance between foci of the setup: 6.4 µm ± 0.1 µm. For each time-step, corresponding to 1 µs, the position of the pattern was translated corresponding to the voltage (V_x, V_y) of the fast-scanning mirror of the setup. V_x and V_y were converted to pixels based on an experimentally determined conversion factor. In each time step the coordinates of the foci were convoluted by the excitation point spread function ($\mathrm{PSF_{exc}}$). PSF_{exc} was approximated by a two-dimensional (2D) Gaussian profile with width (σ_{exc}) based on the numerical model of Richards and Wolf[37] Which state that for objectives with NA>0.7, the estimate of a squared Gaussian profile best fits with a slight inverse power dependence of 0.91:

$$\sigma_{\mathrm{exc}} = \frac{0.65\,\lambda}{\mathrm{NA}^{0.91}} \tag{4.3}$$

A map of the effective exposure time for each pixel ($\mathrm{M_{exp}}$) was computed by integration of the intensity of each pixel over all time steps during one exposure. This was combined with a map of randomly distributed molecules on a 2D surface (M_{sample}). A fluorescence image ($M_{fluorescence}$) was calculated according to:

$$\mathrm{M_{fluorescence}} = \mathrm{q}\,\mathrm{M_{sample}}\mathrm{M_{exp}}\ \mathrm{p\,R\,P_{focus}}^{2} \tag{4.4}$$

with power per focus P_{focus} in W/cm^2, the repetition rate of the laser R, q the quantum efficiency of rhodamine 6G (q=0.95)[14], and p the probability of two-photon excitation per pulse per Watt/cm^2. p was defined as[38]:

$$\mathrm{p} = \frac{0.588}{2}\,\sigma^{(2)}\tau\left(\frac{1}{\mathrm{R}\tau}\frac{\lambda}{\mathrm{hc}}\right)^{2} \tag{4.5}$$

with $\sigma^{(2)}$ the two-photon absorption cross-section of a fluorophore (in cm^4 s photon^{-1}), τ the pulse width (in fs), h Planck's constant, c the speed of light. At an excitation wavelength of 0.83 µm we used $\sigma^{(2)} =$ 100 cm^4 s photon^{-1} for rhodamine 6G in methanol[14]. Convolution of $M_{fluorescence}$ with the emission PSF (σ=0.4 µm) gives the 2D image with the diffraction limited signals ($\mathrm{M_{signal}}$).

The amount of signal was corrected for the collection efficiency of the setup:

$$\mathrm{I_{image}} = \mathrm{M_{fluorescence}}\,\eta_{\mathrm{objective}}\,\eta_{\mathrm{path}}\,\mathrm{q_{cam}} \tag{4.6}$$

where I_{image} is the actual signal detected by the camera. η_{obj} is the collection efficiency of the objective, η_{path} the transmission efficiency of the emission path, and q_{cam} the quantum efficiency of the camera. For our camera, $\mathrm{q_{cam}} = 0.93$, as specified by the manufacturer. The collection efficiency for a 1.49 NA objective is 0.42. η_{path} was calculated by multiplication of the transmission coefficients of the filters in the emission path and an additional factor of 0.96 per lens surface, which results in $\eta_{path} = 0.55$. Overall, the detection efficiency was $\eta_{setup} = 0.21$, for a wavelength of 500 nm.

For the final image (I) noise factors were added:

$$\mathrm{I} = \mathrm{Poisson}(\mathrm{I}_{\mathrm{signal}}) + \sigma_{\mathrm{dark}} + \sigma_{\mathrm{read}} \tag{4.7}$$

where the Poisson distribution of I_{signal} accounts for shot-noise, σ_{dark} is the Poisson distributed dark-noise of the camera and σ_{read} the Poisson distributed read-noise of the camera. Simulated images were processed using the same software as the experimental data.

Spot detection. The locations of peaks in the fluorescence images were extracted iteratively, starting with the maximum intensity in the image. A circular mask of 7 pixels x 7 pixels was used to block the signal around the found pixel, after which the next pixel with the highest intensity was located. This iterative process was continued until a pixel intensity lower than the mean intensity of the image plus three times the standard deviation of the background was reached.

Signal-to-noise ratio. For each detected spot a circular shaped region of interest (ROI) of 5 pixels diameter was summed to calculate the signal-to-noise ratio (SNR):

$$\mathrm{SNR} = \frac{\mathrm{I}_{\mathrm{signal}} - \mathrm{I}_{\mathrm{background}}}{\sigma_{\mathrm{background}}} \tag{4.8}$$

with I_{signal} the integrated intensity of the ROI. A second doughnut shaped ROI with the same area as the first ROI was used to calculate $I_{background}$ and $\sigma_{background}$.

Bleaching curves. For extracting the bleaching times (τ_{bleach}), $I(t)$ was fitted to an exponential function:

$$I(\mathrm{t}) = \mathrm{I}_0 \mathrm{e}^{-\mathrm{t}/\tau_{\mathrm{bleach}}} + \mathrm{c} \tag{4.9}$$

with I_0 the initial intensity and c the offset.

Single molecule tracking and mean squared displacement (MSD). Spots from the movies of eGFP-HRas measurements were located using TrackMate software as bundled with the Fiji distribution package of ImageJ[39]. The image was median filtered and a Laplacian to Gaussian (LoG) detector was used to filter the image on blob sizes with an estimated diameter of 0.5 µm. Blobs with an intensity lower than 3 times the standard deviation of the background were discarded. A simple linear assignment problem (LAP) tracking algorithm was used to link the detected spots. We set the maximum distance for spot-linking and the maximum gap-closing distance at 0.6 µm, the maximum frame gap between spots was set to 5 frames. After spot-linking, the shortest 10% of all traces were discarded.

The remaining time traces were exported to the open source Icy software. Using the incorporated Track Manager, trace coordinates were converted to a MSD per time-unit t_{lag}. All MSD curves were averaged over all traces, and the confinement length (L) and diffusion coefficient (D) were extracted from the data by fitting a confined displacement model:

$$\mathrm{MSD}\left(\mathrm{t_{lag}}\right) = \frac{\mathrm{L}^2}{3}\left(1 - \exp\left(\frac{-12\mathrm{D_0 t_{lag}}}{\mathrm{L}^2}\right)\right) + \mathrm{A} \tag{4.10}$$

with the initial diffusion constant D_0 and a fixed offset A set at 0.005.

4.3 RESULTS

4.3.1 SINGLE MOLECULE FLUORESCENCE BY SPIRAL ILLUMINATION

First we measured single fluorophores by two-photon spiral illumination. To minimize photo-bleaching, the laser power was attenuated to 1.8 mW per focus by neutral density filters. A region of interest (ROI) from the resulting image is shown in Figure 4.2a and shows randomly distributed diffraction limited spots. To determine whether the spots originated from single fluorophores we continuously imaged at 4 Hz for 60 seconds and checked for discrete bleaching steps. Three representative time traces are plotted in Figure 4.2b. The intensity for all three traces is around 1000 Hz at the start of the measurement. Distinct single bleaching steps, indicative of single molecules, occurred during the measurement which shows that the TPE signal from single fluorophores is readily observed for tens of seconds.

Having established two-photon single molecule fluorescence, we next characterized the signal of all fluorophores. A total of 86 peaks were identified in the first image of the measurement. Bleaching was defined as when the 5 point moving average filtered signal dropped below 1.5 times the average background. The distribution of the signal intensity from these 86 traces and their background is plotted in Figure 4.2c. With a signal of $9 \pm 4 \times 10^2$ Hz (mean ± SD) and an average background of $2.4 \pm 1.1 \times 10^2$ Hz, the signal-to-noise ratio (SNR) for all traces was 4 ± 2. This indicates that the excitation power of 1.8 mW per focus in combination with 200 ms integration time, is sufficient to detect single fluorophores with sufficient SNR. We observed a larger variation ($\sigma = 4 \times 10^2$ Hz) in intensity than we would expect from a shot-noise limited signal ($\sigma = 0.5 \times 10^2$ Hz). These larger fluctuations could arise could from instability of the fluorophores. The corresponding time before bleaching is plotted in Figure 4.1d. The distribution of bleaching times was fitted to an exponential decay function (equation 4.9), yielding an average bleaching time of 17 ± 2 seconds. A large number of peaks did not bleach during 60 seconds of imaging, but these were not processed due to poor SNR. The presence of these weak fluorescent signals after 60 seconds suggests a non-homogeneous excitation pattern and that these fluorophores received less illumination than the fluorophores displayed in Figure 4.2. Though these measurements show that it is possible to image single fluorophores in wide-field with TPE *in vitro*, for biological applications *in vivo* the demands are tougher, partially due to the increased background.

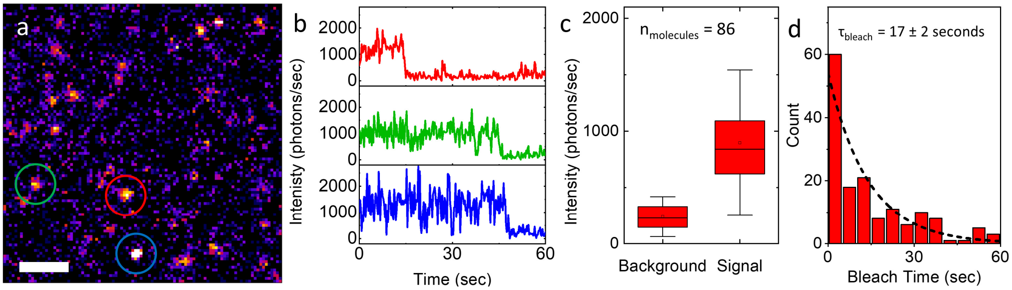

Figure 4.2: **Two photon image of single rhodamine 6G molecules imaged in wide-field.** (a) A wide-field image of individual rhodamine 6G molecules on a glass surface. Sample is illuminated by spiral-scanning of multiple foci. Scale bar = 5 µm. (b) Time traces of the fluorophores as indicated by color from *a*. Single bleaching steps indicate that signal originates from a single fluorophore. (c) Distribution of the background and signal of single molecules. Single molecules are resolved with an average SNR of 3.5. d) Distribution of the bleach times from 86 individual fluorophores. Distribution is fitted to an exponential, yielding a half-time ($t_{1/2}$) of 16.5 seconds.

4.3.2 BACKGROUND REDUCTION BY SLIM

Reducing the background signal is important for better contrast images, and indirectly for extending the bleaching time because it allows for lower excitation power. To investigate the ability of SLIM to reduce the background intensity *in vivo*, we imaged blood vessels inside the brain of three-day old zebrafish embryos. The embryos expressed mTurquoise in endothelial cells by fusion of the fluorescent protein to the vascular growth factor *kdrl*. Figure 4.3a shows a cross-section of a blood vessel approximately 40 µm inside the embryo imaged by spiral illumination. The SLIM image in Figure 4.3b is of the same location as Figure 4.3a. As opposed to the SLIM image, in the spiral scanning image there is substantial intensity in the center of the blood vessel. Also on the right of the blood vessel there is a large area which features enhanced brightness. As both image modalities optically dissect the sample via TPE, this signal cannot be attributed to out of focus excitation, and is therefore likely the result of scattered fluorescent signal. A ROI from Figure 4.3a (white square) is shown in Figure 4.3c. The image displays the higher fluorescence in the blood vessel more clearly. In the annotated ROIs (dotted white lines) the average intensity inside was 205 ± 62 Hz and outside the blood vessel it was 93 ± 29 Hz. We compared the background found here with the signal we measured for single rhodamine 6G molecules on glass using the same illumination settings. For this, we divided the average intensity of 900 Hz from Figure 4.2c by the 5 x 5 mask size from which that signal was integrated, this yields an intensity per pixel of 36 Hz. Note that the peak intensity of a spot was typically three times higher. The average intensity is lower than the background intensity of the *in vitro* measurements, suggesting that spiral illumination would hardly be able to resolve TPE single molecule fluorescence in zebrafish embryos. At the same location for the SLIM image, shown in Figure 4.2f, the background is 14 ± 26 Hz inside and 15 ± 17 Hz outside the blood vessel. In both cases, the reduction in background suggests that it would be possible to detect single fluorophores *in vivo* using TPE.

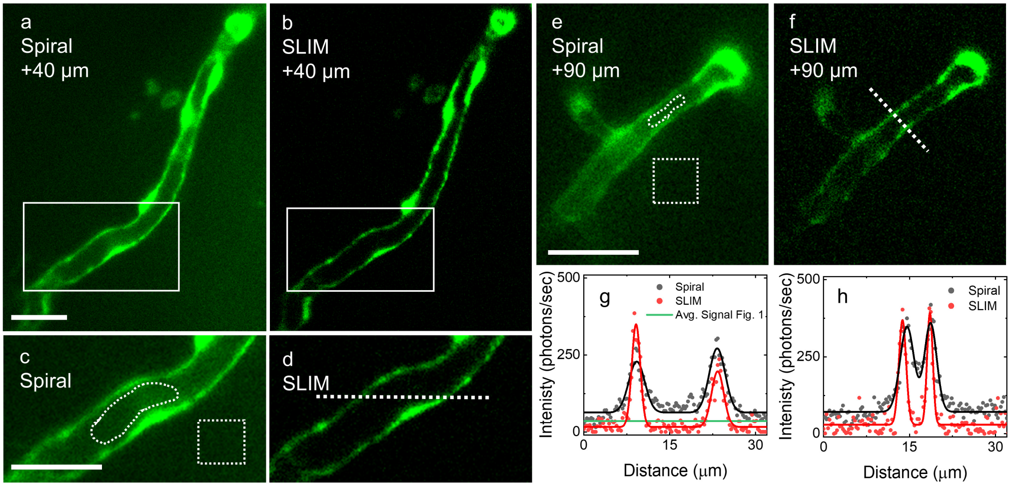

Figure 4.3: Structured illumination reduces scattered light to improve background in *in vivo* environments like the brain of zebrafish embryos. (a) A cross section of a blood vessel imaged via spiral illumination approximately 40 µm inside the embryo. The nuclei are indicated by the thicker and brighter areas of the blood vessel. Scattered light is visible even at larger distances away from the vessel. (b) Imaging the same FOV as in *a* now with SLIM yields a clear reduction in background noise across the image, while retaining signal from the blood vessel. (c) Zoom-in on a blood vessel as annotated in *a* (white square). Background is higher inside the blood vessel compared to the outside. (d) Zoom-in on the annotated ROI in *b* (white square). SLIM clearly reduces background both out- and inside the blood vessel. (e) Cross-section of a blood vessel imaged via spiral illumination located at approximately 90 µm inside the brain. Background appears brighter inside the thinner blood vessel. (f) Even at larger depths SLIM is able to reduce background to a minimum. (g) Comparison between the intensity profiles as annotated in *d* (dotted white line). The boundaries of the blood vessel are clearly visible by two peaks. SLIM reduces background in the blood vessel to the same level as outside the blood vessel. For reference, a line is drawn that indicates the average signal of single fluorophores on glass from Figure 4.2. (h) Intensity profiles from the cross section as annotated in *f* (white dotted line). Again SLIM reduces the background inside the blood vessel to similar level as outside the blood vessel. Also, the blood vessel walls are imaged much sharper in SLIM compared to spiral. Scale bars = 25 µm.

Besides the lower background, the SLIM image features thinner blood vessel walls than the spiral image, as can be seen from the profile plots in Figure 4.3g. Fitting Gaussian functions to the peaks gives a full-width-at-half maximum (FWHM) of 3.3 ± 0.2 µm for both peaks in the spiral image, and 1.8 ± 0.1 µm and 2.5 ± 0.2 µm in the SLIM image. The sharper defined boundary of the endothelial cells quantifies the better resolution due to the suppression of scattered photons. We also imaged blood vessels 90 µm inside the brain. The spiral image of this section is shown in Figure 4.3e and the SLIM image in Figure 4.3f. Similar to the images captured closer to the objective, SLIM reduces background signal significantly. From annotated ROIs (white dotted lines) we find that the background signal inside the blood vessel is reduced from 207 ± 48 Hz to 27 ± 24 Hz when illuminating with SLIM as compared to spiral scanning. Background signal inside the blood vessel is higher compared to the more superficial vessel. Still, SLIM drastically reduced background signal at 90 µm imaging depth, with a background below single molecule intensities. The increased absorption and scattering of emission photons however, may complicate the detection of single molecules at these depths. The higher background is likely caused by the narrower blood vessel which increases the possibility of including signal of the top or bottom of the vessel. Outside the blood vessel SLIM does reduce background to 11 ± 17 Hz, which is similar to that of the superficial vessel. The intensity profiles (dotted white line, Figure 4.3f) for the spiral and SLIM images are plotted in Figure 4.3h. The profile plots clearly show that SLIM is able to image the blood vessels sharper, which translates to a reduction in background signal inside the vessel as there is no overlap between signal from the blood vessel walls. From fitting Gaussian profiles in the spiral image, we find that the FWHMs of the blood vessel walls are 2.9 ± 0.2 µm and 2.5 ± 0.1 µm. In contrast, in the SLIM image they are 1.4 ± 0.1 µm and 1.2 ± 0.1 µm – a reduction of more than two.

Besides attenuating scattered emission photons, SLIM may also help to reduce reflected excitation light from the laser. Due to the difference in wavelength, and hence the difference in PSF of the excitation and the emission light, this may be especially effective for out-of-focus reflections, for example at the interface between the bottom of the slide and the immersion liquid. The ability to suppress back-reflected light relaxes the necessity for spectral filters in the emission path which will increase the collection efficiency of the setup. To demonstrate this, we imaged rhodamine-5-molecules incorporated in a DNA construct that was immobilized on a glass surface. To facilitate detection an average of 9 rhodamine molecules were incorporated per DNA molecule. To enhance the contribution of reflected light we removed one of the band pass filters in the emission path and imaged the sample by spiral scanning and SLIM, the results are shown in Figure 4.4a and 4.4b. Without the second emission filter, the excitation area can be clearly distinguished by the increased background signal in the middle of the spiral image. Inside the excitation area, spots of higher intensity indicate the location of DNA rhodamine. Although the DNA molecules are clearly discernable, the increased background compromises the signal to background ratio. Note that the difference in intensity between the spots likely originates from variations of the number of rhodamine fluorophores per DNA molecule or perhaps even from aggregates of DNA. Switching to SLIM, the reflections from the laser are indeed significantly reduced and DNA rhodamine is clearly visible in the reduced background.

We compared the background for both illumination modalities by plotting the average intensity inside annotated ROIs (white squares). With two band pass filters, spiral and SLIM have a similar average background of 20 ± 21 Hz and 17 ± 24 Hz, respectively. The background increases around a factor of 4 to 80 ± 26 photons/second when a band pass filter is removed in spiral imaging. In contrast, the SLIM image retains a low background at 13 ± 25 photons/second. We confirmed suppression of scattered photons in simulations, see Figure S4.1. The simulations show how SLIM is less affected by an increasing background signal compared to spiral illumination. Interestingly, the simulations suggest that in absence of reflected laser light, spiral illumination is able to resolve more single fluorophores and at a higher SNR. Still, from these results we can conclude that SLIM is effective to remove reflected of light from the laser, which allows for more efficient detection of fluorescence and could be useful for single molecule detection.

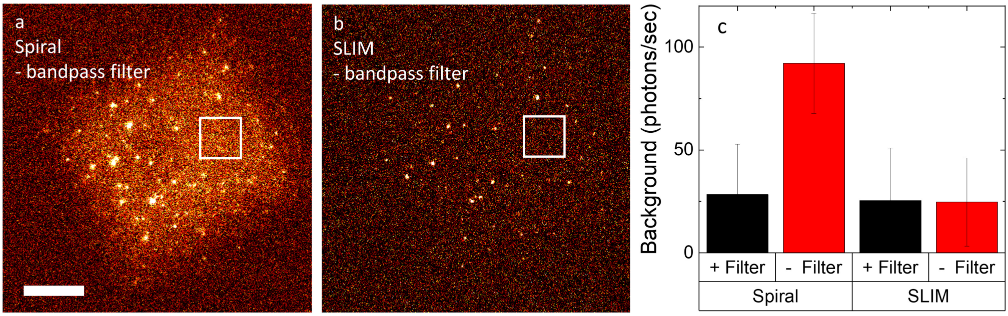

Figure 4.4: Reflected light is removed from the image by SLIM. (a) DNA tethered on glass loaded with an average of 9 rhodamine B molecules imaged via spiral scanning. By removing a band pass filter in the emission path laser light adds a high background intensity. Scale bar = 10 µm. (b) SLIM image of the same FOV and with similar imaging conditions as *a*. Background is reduced to the level outside the excitation field, while the DNA-rhodamine spots are still visible. (c) Comparison of the background of both illumination modalities with and without bandpass filter. Spiral scanning increases the average background 3.7 times while SLIM remains at similar levels.

4.3.3 SIMULATIONS

We simulated single molecule experiments for both spiral and SLIM illumination to better understand how SLIM could improve single molecule studies. First we studied the influence of the number of phase-images on single molecule detection. From the *in vivo* measurements in zebrafish embryos we noticed that SLIM results in less homogenous illumination than spiral scanning, see Figure S4.2. Due to the non-linear excitation, this may be more problematic for two-photon imaging than for one-photon imaging. In the simulations, randomly generated locations of fluorophores were convoluted with a Gaussian profile with a width of 0.4 µm to act as the ground truth image of the fluorophores, shown in Figure 4.5a. The same fluorophore coordinates were used in the spiral- and SLIM simulations for direct comparison between the images. Spiral scanning was simulated with the same parameters as used in the experiments, while for SLIM the number of phase images was varied from 1 to 9.

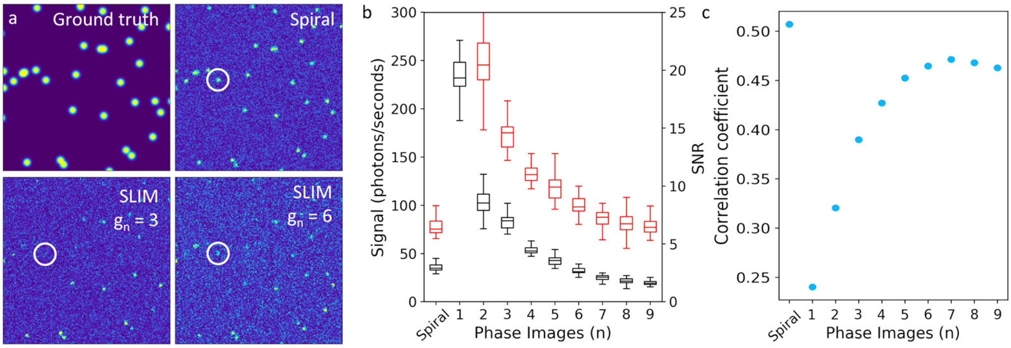

Figure 4.5: Theoretical comparison of spiral scanning and SLIM microscopy. For SLIM the number of phase-images has a large effect on the resulting image. Spiral scanning yields a better representation of all fluorophores while SLIM produces higher SNR. (a) ROI of an input image showing a distribution of fluorophores. The spiral image captures all fluorophores, whereas some fluorophores in the SLIM images are hardly visible. (b) The signal intensity (red) and SNR (black) of 150 fluorophores from each simulation. The small variation in signal intensity from spiral scanning indicates a homogeneous illumination across the image. SLIM under-samples the image which results in large variations in signal intensity. For seven phase-images or more, signal comes close to that of spiral images, but SNR decreases however. (c) Correlating the images with the ground truth provides a measure on how well the image is reconstructed. The higher correlation coefficient of spiral scanning indicates better performance of spiral scanning for imaging fluorophores. At n=7, correlation is highest in SLIM reconstruction.

In the simulations, each fluorophore was observable in the spiral image, albeit somewhat obscured by the noise. In the image reconstruction from three phase images, it is clear that SLIM spatially under-samples the FOV, such that many fluorophores were undetected. The fluorophores which were detected are however brighter due to the longer exposure time per image. With eight phase images, the FOV appears to be fully sampled as all fluorophores were detected. However, their signal appeared less bright compared to the spiral image and showed more variation in brightness between the fluorophores. For example, the fluorophore indicated by the white circles is barely visible. To quantify these observations, images were processed similarly as the experimental single-fluorophore data. The SNR of 150 fluorophores was calculated. Signal intensity was defined by the amplitude of a fitted 2D Gaussian. The distribution of the peak intensity and the background are plotted in Figure 4.5b. The intensity of the spiral illuminated photons was 76 ± 12 Hz and the corresponding SNR is 2.7 ± 0.2. The relatively small variance indicates a homogenous illumination as the fluorophores receive similar exposure during integration of the camera.

In contrast, SLIM with only a few phase-images results in inhomogeneous illumination and therefore in large variation in signal and SNR. Illumination is distributed more evenly when increasing the number of phase-images. However, doing so decreased the signal and SNR. Using 6 phase images, the SNR is lower than that of spiral illumination. The lower SNR with higher average signal of 98 ± 14 Hz, indicates that a higher variance in background impairs the SNR of the SLIM images. Next to inhomogeneous illumination, this might be explained by additional readout noise per phase-image that would reduce the SNR of the reconstructed SLIM image. To measure the resemblance with the ground truth image, we plotted the amplitude of the cross-correlation between the ground truth image and the simulated images in Figure 4.5c. Despite the 20% higher collection efficiency of SLIM due to the absence of a band pass filter, spiral scanning had the highest correlation coefficient. SLIM had a maximum correlation at 7 phase-images.

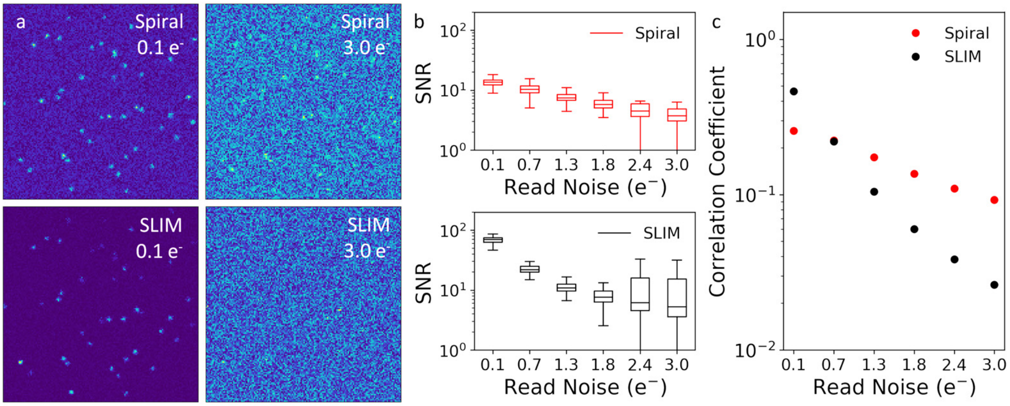

Figure 4.6: Simulations to study the influence of read noise on imaging single fluorophores for spiral scanning and SLIM. (a) Four ROIs for both illumination modalities at two different noise levels. At 0.1 e^- read noise spiral scanning and SLIM perform similar, while at 3.0 e^- fluorophores can hardly be observed in the SLIM image. (b) SNR for the spiral and the SLIM simulations. At 0.1 e^- the SNR of SLIM is higher, however it drops rapidly when the read noise is increased. The large standard deviation of the SNR for SLIM impedes detection of fluorophores. (c) Correlation coefficients for spiral and SLIM at different read noise levels. SLIM suffers more from a higher read noise than spiral scanning. These results show that the read-noise from multiple separate phase images result in a poorer performance of SLIM compared to spiral scanning.

The decrease in SNR when using more than 7 images for SLIM reconstruction suggests that camera read-out noise, which is a random signal that is generated each time a frame is acquired, may become the largest contributor to reduced image quality. To test this, we simulated spiral and SLIM measurements at different levels of camera readout noise. With 0.1 e^- readout noise both spiral and SLIM can easily discriminate fluorophores from the background, as shown in Figure 4.6a. At 3.0 e^- noise, no clear peaks are observed with SLIM, while in the spiral image most peaks are still above the noise floor. The trend in SNR when read noise is increased is plotted in Figure 4.6b. SLIM suffers significantly from more read noise compared to spiral. Interestingly, at 0.1 e^- SLIM achieves higher SNR than spiral scanning, where external scattered signal is dominant over read noise. The correlation coefficient, plotted in Figure 4.6c, shows a similar trend as the SNR. At minimal read noise SLIM is able to capture the distribution of fluorophores better than spiral illumination. However, as read noise becomes dominant, the correlation coefficient of SLIM decreases exponentially, with a rate 2.7 faster than the spiral simulations. Why SLIM is more effected by read noise might be explained by the less signal which is collected per phase-image compared to a spiral image. With less signal and increasing noise, the SNR per phase-image decreases more rapidly compared to spiral scanning, which would translate into worse SNR of the reconstructed SLIM image. The median of the read noise of the camera used in our experiments is 1.1 e^- as stated by the manufacturer. Based on these simulations with a low scattering background (0.5 e^-/second), spiral illumination would be the preferred illumination modality.

4.3.4 TWO PHOTON BLEACHING RATES

Suppression of background and removal of the band pass filter for higher collection efficiency, can be used to lower the excitation power while maintaining a similar SNR compared to spiral illumination. A reduction in excitation power is important for less photo-toxicity and reduced photobleaching. To clarify the relation between excitation power and bleaching, we measured the reduction in fluorescence over time when continuously imaging a dense layer of rhodamine 6G deposited on a glass coverslip. The summed intensity of a region of interest is plotted in Figure 4.7a. To extract the bleach rate (τ_{bleach}) we fitted a mono-exponential decay (equation 4.9) and plotted the bleach time as a function of excitation power on a log-log scale in figure 4.7b. At 1.8 mW excitation power the average bleaching time of 17 seconds, as found for single rhodamine molecules, is shorter than the 26 seconds found here in Figure 4.2d. We attribute this to a difference in the position of the focus relative to the fluorophore. Fitting a power law to τ_{bleach} yielded a slope of 2.5 ± 0.1. The initial intensity of the bleaching curves is also plotted in Figure 4.7b and fitted to a slope of 2.0 ± 0.1, confirming two-photon excitation.

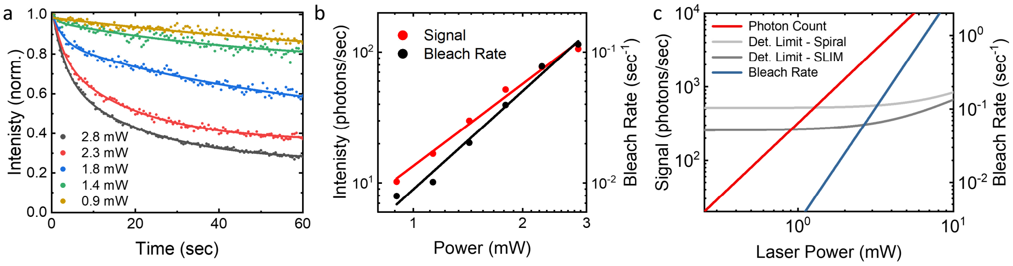

Figure 4.7: Photo-bleaching scales faster than signal intensity as functions of laser power. (a) Photobleaching of a layer of rhodamine 6G deposited on a glass coverslip. Measurements were performed at different excitation powers and fitted to an exponential function. (b) The decay times obtained from *a* plotted as a function of excitation power. The bleaching rates are fitted to a linear function yielding an exponent of 2.5. The signal intensity at the start of each scales with an exponent of 2.0, as expected for two-photon excitation. (c) Theoretical photon count, detection limit and bleach rate as a function of laser power. Bleach rate is obtained from *b.* As excitation power increases, the bleach rate scales unfavourably with laser power. Therefore, background suppression and higher detection efficiency of SLIM could potentially decrease bleach rates while maintaining similar SNR.

The higher slope of the bleaching curve suggests a multi-photon process for bleaching, possibly the absorption of another photon after two-photon excitation. In any case, longevity of a fluorophore increases more with less excitation power than the fluorescent signal decreases, suggesting that bleaching becomes less problematic when background can be reduced, allowing for lower excitation intensities. This relation between SNR and bleach time is plotted in Figure 4.7c, together with the measured bleach rate, the theoretical signal intensity of rhodamine 6G (equation 4.4) and the detection limit (equation 4.5). For spiral illumination an additional noise level of 6.0 photons/second was added to include the increased scattering in *in vivo* environments. For SLIM illumination, the transmission efficiency of the emission path was increased by 21%, which can be achieved by removal of a band pass filter.

A theoretical fluorescent signal of 1400 Hz is expected for single molecules, which slightly deviates from the measured intensities in Figure 4.2 of 897 ± 215 Hz. Inaccuracies in the estimation of the detection efficiency may be the cause for this difference. For spiral scanning, the signal only exceeds the detection limit at an excitation power of 1.05 mW, which results in a bleach time of 450 seconds. For SLIM, signal exceeds the detection limit at 0.8 mW excitation power, which corresponds to a bleach rate of 2500 seconds. Thus, a reduction of 0.69 in power extends bleaching by more than a factor of 5. From these results we expect that single fluorophore studies can benefit from TPE SLIM for both *in vitro*, by the increased transmission efficiency, and in *in vivo* environments, by suppression of scattered photons.

4.3.5 SINGLE MOLECULE FLUORESCENCE BY SLIM

To compare single molecule imaging by SLIM with spiral illumination, the same sample with single rhodamine 6G molecules was measured at an excitation power of 1.8 mW per focus. The band pass filter was removed from the emission path to improve detection efficiency. A ROI from the resulting image is shown in Figure 4.8a. Three diffraction limited spots are identified from the image and annotated by the colored circles. Single bleaching steps in the time traces, shown in Figure 4.8b, confirm that signal originates from single fluorophores. However, the density of observed fluorophores is much smaller compared to the spiral illuminated sample in Figure 4.2a.

From the entire image, a total of 16 fluorophores were detected compared to 86 with spiral illumination. Thus we overlooked 80% of the molecules. The average intensity of detected fluorophores however, is higher with 1480 ± 787 photons/second, as plotted in Figure 4.5c. When fluorescence is lost an average background signal of 509.9 ± 276 photons/second is recorded. Based on the background and average signal, fluorophores are detected with SNR = 2.9, which is slightly less than spiral illumination (SNR = 3.5). Besides SNR, the bleaching time of 14 ± 2 seconds, as plotted in Figure 4.8d, is also comparable to the bleaching time recorded in Figure 4.2d of 17.5 ± 1.7 seconds. So surprisingly, *in vitro* SLIM yields single molecule measurements with similar quality as spiral scanning but a large number of fluorophores remain undetected.

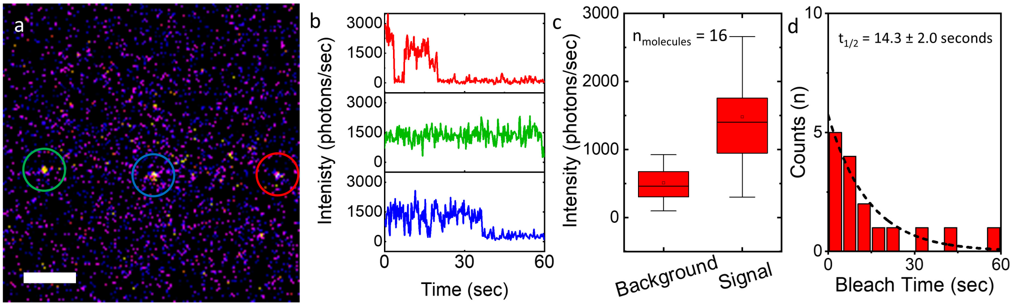

Figure 4.8: Two-photon SLIM imaging single rhodamine 6G molecules. (a) ROI showing single Rhodamine B molecules deposited on a glass coverslip. Scale bar = 5 µm. (b) Time traces of the displayed fluorophores in *a*. Discrete bleaching steps indicate single fluorophores. (c) Average distribution of the background and signal of single 16 fluorophores. Based on the mean values, a single fluorophore is resolved with a SNR of 2.9. (d) The distribution of the bleach times yields a half-time of 14.3 seconds.

4.3.6 ENHANCED SLIM (SLIM+)

To tackle the high readout noise and enhance single molecule visibility we reduced the number of phase-images for one SLIM acquisition. This was achieved by scanning three lines during one phase-image, thereby broadening the resulting excitation pattern compared to conventional SLIM, see Figure 4.9a. The broader lines in the enhanced SLIM configuration reduced the number of phase images from eight to three. To assess the performance of SLIM+ we simulated single molecule measurements at different background intensities and compared SLIM+ to conventional SLIM and spiral illumination. The resulting images were cross-correlated with the ground truth to assess which illumination modality provides highest fidelity results, see Figure 4.9b.

The correlation coefficient of SLIM+ is significantly higher than SLIM and except for 0.3 photons/sec noise, is also higher than spiral illumination. This indicates that SLIM+ is superior to spiral scanning for most measurements. The slope of the correlation coefficient for SLIM+ is steeper compared to SLIM which suggests that for higher scattering media SLIM would perform better. This is likely caused by inefficient signal modulation at higher background in SLIM+ due to the broader illumination lines. Besides higher correlation, SLIM+ roughly doubles the SNR compared to spiral and SLIM illumination at a background intensity of 2 photons/sec, as shown in Figure 4.9c. Besides better quality images, the reduction in phase-images also reduced the file size of a measurement and allowed for faster imaging as less time is spent on reading-out the camera buffer. But most importantly, the higher SNR especially shows how the reduction in readout noise is beneficial for single molecule tracking. SLIM+ eliminates most of the drawbacks of SLIM.

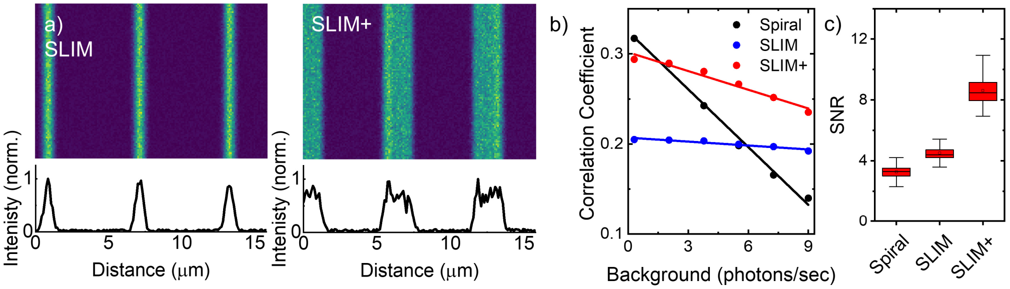

Figure 4.9: Reducing the number of phase-images improves image quality for SLIM. (a) Simulated excitation-images of SLIM and SLIM+. By scanning three lines per phase-image, the width of the resulting streak is broadened. With only three phase-images the FOV is fully sampled, reducing camera readout noise. (b) The correlation coefficient is improved by SLIM+, indicating that more fluorophores are resolved compared to SLIM. For high background images, SLIM+ performs better than spiral scanning. c) Due to the reduced readout noise the SNR is doubled by using SLIM+ compared to SLIM.

4.3.7 *IN VIVO* SINGLE MOLECULE FLUORESCENCE

Next we tested whether the improvements of SLIM+ made it possible to measure single fluorophores in live zebrafish embryos. For these measurements the membrane protein HRas was fluorescently tagged at its CAAX anchor domain with an eGFP fluorescent protein. The membrane of the skin cells in the tail of the embryo, shown in Figure 4.10a, were imaged using a spiral illumination. The boundaries of the cells can be distinguished by their distinct pentagonal shape. Homogenous intensities of the diffraction limited spots suggest single fluorophores. Note that we hardly observed photobleaching, the hallmark of single molecule fluorescence. We validated our results by comparing our SLIM+ images to measurements done with the well-established single molecule imaging technique of TIRF microscopy, see Figure S4.3. The two images both feature diffraction limited spots originating from HRas proteins. Within each image the spots feature comparable signal intensity and the similarities between both imaging modalities indicate that TPMM signal originates from single fluorophores. The background signal was greatly reduced when switching to SLIM+ as shown in Figure 4.10b. This can also be seen in the increase of SNR between the images as plotted in Figure 4.10c. The median SNR of the spiral image was 4.3 while the median of the SLIM+ image was 7.1, a factor of 1.6 improvement. Besides higher positional accuracy, a higher SNR allows to increase image speed or reduce excitation power to reduce phototoxicity and photobleaching.

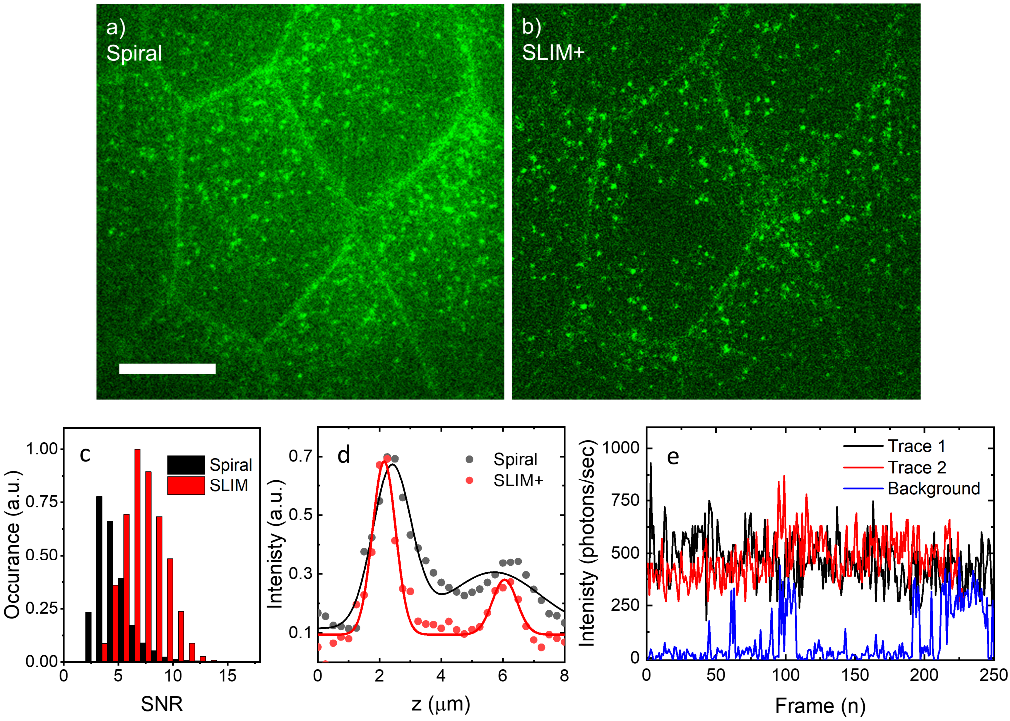

Figure 4.10: In live zebrafish embryos SLIM+ achieves higher SNR and improves the axial resolution compared to spiral scanning for imaging single molecules. (a) Spiral image of skin cells in the tail of a zebrafish embryo. eGFP labelled HRas proteins located in the cell membrane are clearly distinguishable. Scale bar = 10 µm. (b) SLIM+ image of the same location as *a.* The suppression of background improves the visualization of single eGFP-HRas proteins. (c) SNR calculated from the diffraction limited spots according to eq. 4.8. Spiral illumination reveals eGFP-Hras proteins with a median SNR of 4.3. SLIM+ improves SNR nearly 2-fold to 7.2. (d) Line profiles of a z-stack of the imaged cells. The first peak is the bottom membrane, the second peak, ±4 µm deeper, reveals the top membrane. Due to suppression of scattered photons in SLIM+, the membrane can be imaged at a higher axial resolution compared to spiral illumination. Fitting a double Gaussian yields a FHWM of 0.88 ± 0.06 µm for the first peak with SLIM+ and 0.94 ± 0.20 µm for the second peak. For the spiral z-stack: FWHM = 1.5 ± 0.1 µm and 3.5 ± 0.7 µm. (e) Intensity time trace of two tracked traces and a static region of interest. Note that the absence of photobleaching enabled tracking of the molecules for extended periods of time.

Next we assessed whether the Hras spots were confined to the membrane by measuring their position in 3D. ROIs of 69 x 79 pixels for both spiral and SLIM + images were taken from inside the center cell and the average signal of their z-profile are plotted Figure 4.10d. The two cell walls can be clearly distinguished from the two peaks, indicating that fluorescent signal is exclusively present in the membrane. Fitting a double Gaussian to the SLIM+ profile yields a FHWM = 0.88 ± 0.06 µm for the first peak and 0.94 ± 0.20 µm for the second peak. In comparison, the peaks in the spiral image feature a FWHM = 1.5 ± 0.1 µm for the first- and 3.5

± 0.7 µm for the second- peak. The suppression of background signal yields a much thinner cell membrane, and limited fluorescence degradation in axial resolution for the top membrane.

Most notably is the limited photobleaching we observed during these measurements. We set camera integration time at 100 ms and imaged for hundreds of frames using SLIM+ yielding movies lasting up to five minutes. Using TrackMate software combined with a simple linear assignment problem (LAP) tracking algorithm[39], individual spots of single molecules were tracked for hundreds of consecutive frames. Two examples of the resulting intensity traces are shown in Figure 4.10e. To compare to the background signal we also plotted the average signal from a static ROI in the middle of the cell with the same diameter (0.53 µm) as the traced spots. The spikes in intensity at the end indicate fluorophores passing through this region as HRas proteins diffuses through the membrane. We expect the detected intensity from each single molecule to be the same. Indeed, trace 1 and trace 2 both feature a similar average signal intensity of approximately 500 Hz. Also the spikes in the background signal reach similar levels of intensity. Lower intensity spikes are the result of molecules passing through the edge of the ROI. Trace 2 disappears after 225 frames which indicates that the fluorophore is bleached, the molecules moves out of focus, or the tracking algorithm is unable to link the consecutive frames. It is difficult to assess the reason behind the disappearance of a trace while they are moving in an *in vivo* environment. These results show how TPMM in combination with structured illumination enables the *in vivo* visualization of single molecules with limited photobleaching and negligible background signal.

4.3.8 ANALYSIS OF *IN VIVO* SINGLE MOLECULE DYNAMICS

Having established *in vivo* single molecule imaging with TPMM, we next investigated its functionality by tracking eGFP-HRas proteins in live zebrafish embryos. We used both spiral and SLIM+ illumination modalities to assess how they compare. To quantify this, we defined two ROIs: ROI 1 near the lateral membrane of the cell and ROI 2 at the center of the bottom membrane of the cell, shown in Figure 4.11a. The limited photobleaching allowed us to automatically track molecules by TrackMate software[39] for tens of seconds in a one minute movie. From the trajectories in ROI 2, shown in Figure 4.11b, we see that most traces are relatively short and some molecules reside for longer time periods within a confined area. These trajectories comply with out visual inspection. A large population of HRas proteins rapidly traveled across the membrane while sometimes remaining immobile for short periods of time, and a smaller second population appear to reside within a confined area for longer periods.

We studied the temporal-spatial dynamics of HRas by means of their MSD, which was calculated from the tracked coordinates. The MSD for both ROIs are plotted in Figure 4.11c and a confined diffusion model (equation 4.10) was fitted to the data. The variation in confinement between traces was very large, see Figure S4.4a for individual traces, and therefore we focus on the average MSD. The large spread in confinement may justify a more refined, multi-population approach but here we limit the analysis to a simple single population. During the tens of seconds of tracking a molecule could also change its mobility, for example by interactions with its environment, which could also affect the MSD analysis.

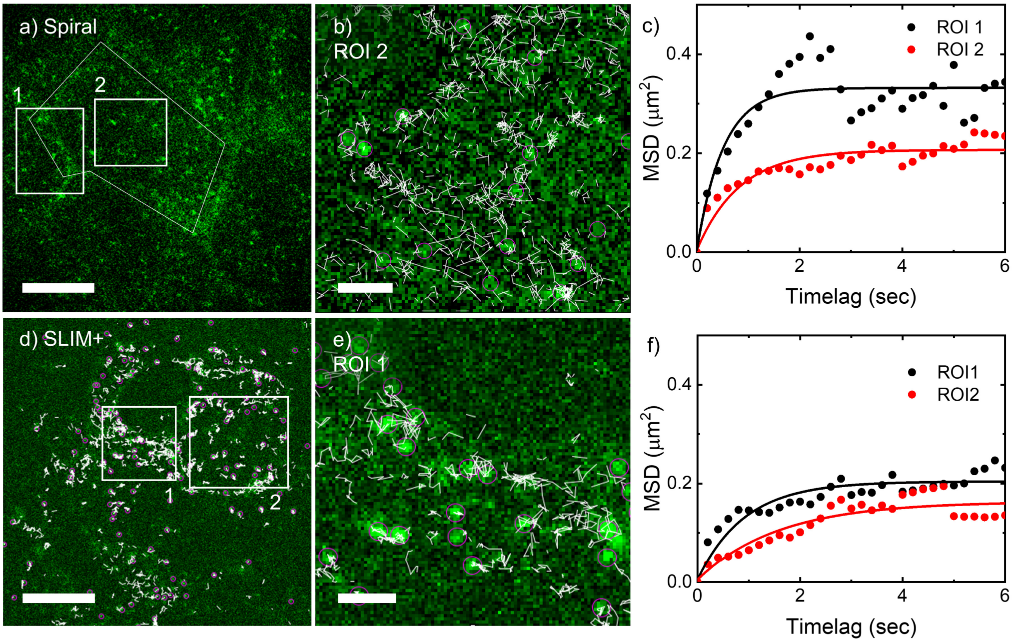

Figure 4.11: HRas proteins in the membrane of live zebrafish embryos feature different dynamics in different regions of the cell. (a) Two ROIs (white squares) annotate areas near the lateral membrane and the centre of the bottom membrane in a spiral-illuminated image. Scale bar = 10 µm. (b) Visualization of the trajectories of several eGFP-HRas proteins in ROI 2. Scale bar = 2 µm. (c) The average MSD calculated from the spatial coordinates of the tracked traces. Fitting a confined diffusion model (eq. 4.10) to the data yields a higher diffusion constant and less confinement for the traces located at the lateral membrane (L = 0.57 ± 0.17 µm) than those located in the interior of the cell (L = 0.46 ± 0.17 µm). (d) A SLIM+ image of embryo skin cells with traces from the tracked molecules overlaid in white. The regions near the lateral cell membranes feature higher eGFP-HRas mobility (ROI 1) than in the centre of the bottom membrane of the cell (ROI 2). (e) Enlarged image of ROI 1 at the lateral cell membrane. (f) Although small, the average confinement for ROI 1 with a L = 0.44 ± 0.10 µm is higher than 0.40 ± 0.14 µm at ROI 2.

Both MSD curves reach an asymptote indicating confinement. The area of confinement is larger near the lateral membrane wall, L = 0.57 ± 0.17 µm than at the bottom of the cell with a L= 0.46 ± 0.17 µm. From HRas measurements using TIRF microscopy at the bottom of the cell membrane we measured L = 0.33 ± 0.17 µm, see Figure S4.4b. The diffusion constants as measured by TPMM of 0.16 ± 0.03 µm^2/sec and 0.06 ± 0.01 µm^2/sec, were smaller than measured in TIRF of 1.68 ± 0.24 µm^2/sec. This could be due to the lower frame rate of TPMM, which may bias our analysis to the slower fraction of molecules. The difference in confinement between the microscopy modalities could be due to the large variation in the traces in TPMM, which would warrant a more refined analysis. However, the enhanced photobleaching of TIRF could also eliminate longer traces which may skew results towards more confinement.

At a different region in the tail of the zebrafish embryo we also used SLIM+ to track eGFP-HRas. The FOV shown in Figure 4.11d features multiple cells. By superimposing the eGFP-HRas trajectories on the image the difference in HRas activity between the different cell regions and cells can be qualitatively appreciated. For example, the area at the top of ROI 1 which features no traces is likely a cell which expresses very limited eGFP-HRas. Similar to the spiral measurement we saw more HRas mobility at a lateral cell membrane (ROI 1) than in the interior of a cell (ROI 2). Figure 4.11e provides a closer view at ROI 1 and similar to Figure 4.11b, shows how some molecules remain longer immobilized at a specific place, while other traces are shorter and/or more mobile. Although we cannot exclude photobleaching, it is unlikely that bleaching is responsible for such short traces as there is no sign of bleaching at the cell membrane nor any part of the embryo (data not shown). More likely eGFP-HRas moves out of focus or the tracking algorithm was unable to link a spot to the trace. From the MSD curves plotted in Figure 4.11f we find that the traces are confined with L = 0.44 ± 1.0 μm for the lateral membrane and 0.40 ± 1.4 μm for the interior of a cell. The variation in MSD traces is again very large. Still, the average area of confinement at the lateral membrane is higher than that at the central bottom of the cell. For both regions the confinement appears to be smaller than in the spiral measurement and resembles the TIRF measurement. The apparent diffusion constant is further reduced to 0.055 ± 0.006 μm^2/sec and 0.025 ± 0.003 μm^2/sec. Differences between MSD values could be caused by biological variations between cells, or by modulations in either spiral or SLIM+ acquisitions. A more rigorous study should be conducted to assess these differences between the two scanning modalities. Besides a higher SNR, as also reported in Figure 4.10, and the slightly different diffusion behavior, we did not see major differences between movies obtained with spiral and SLIM+. Both were able to track single molecules for tens of seconds and provided insight in HRas dynamics across multiple cellular bodies.

4.4 DISCUSSION AND CONCLUSION

In this work we measured wide field two-photon fluorescence of single fluorophores both *in vitro* and *in vivo*. Individual rhodamine 6G molecules on glass were readily imaged with an average life-time of 17.5 seconds. To enhance visibility of single fluorophores and to increase SNR in images overall, we developed SLIM to suppress scattering of photons. The higher background in turbid media, such as of zebrafish embryos, was reduced to below single molecule brightness by SLIM. Moreover, we further improved SLIM to reduce the effect of the increased readout noise and make it suitable for imaging of single fluorophores. Indeed, we imaged single eGFP-HRas proteins in live zebrafish embryos where the absence of bleaching allowed us to track single molecules for sometimes hundreds of consecutive frames.

The fluorophores immobilized on glass which were detected by spiral illumination, had an average signal of 900 Hz at a relative low excitation power of 1.8 mW. TPSM on rhodamine B[13] shows similar bleach rates as rhodamine 6G, indicating that imaging these fluorophores with TPMM would yield similar results for *in vitro* environments. When compensated for difference in illumination intensity measured by TPSM (our 410 kW/cm^2 versus 1340 kW/cm^2) and scan speed (9.4 ms/pixel versus 0.2 ms/pixel), our results closely follow the power dependence on the bleach rate of single rhodamine 6G molecules[14]. However, the frame rate of TPMM is 5.6 times higher. To achieve a similar frame rate while maintaining SNR, TPSM would need to scan 5.6 times faster and thus required approximately 2.4 times larger excitation power, which would decrease bleaching times to approximately 2 seconds. For practical imaging purposes this comparison indicates that TPMM indeed offers lower bleaching times than single point excitation.

The photobleaching times of eGFP molecules inside the zebrafish embryo were significantly different to rhodamine 6G on glass, with molecules that could be tracked for over one minute. These drastically different results were achieved at a slightly lower excitation power of 1.6 mW for *in vivo* versus 1.8 mW for the *in vitro* measurements. The small difference here in power is unlikely to cause an order of magnitude difference in bleaching times but the different fluorophores have different bleaching behavior.

The exact two-photon bleaching mechanisms of fluorescent proteins remains elusive. Fluorescent correlation spectroscopy (FCS) measurements showed that the two-photon photobleaching rates of fluorescent dyes and proteins were not influenced by the addition or removal of solvated oxygen to the imaging medium, whereas in one-photon excitation oxygen strongly increases bleach rates[40]. Moreover, TPE did not appear to induce significant triplet-state formation, which is one of the main oxygen dependent bleaching pathways of one-photon excitation. These results suggested that the two-photon photobleaching process differs significantly with one photon excitation. TPE may induce higher-order excited-states, e.g. three-photon absorption, which could lead to destruction of fluorescence by formation of an ion pair between the fluorophore and a solvated electron[41–43]. This effect can be countered by adding stabilizing agents such as ascorbic acid, which non-destructively deoxidizes the excited fluorophore[40]. Interestingly, the bleach rate of eGFP does not respond to ascorbic acid and was previously found to be remarkably stable upon TPE [40,44]. The tight cylinder of amino chain acids is believed to shield the fluorescent center from reactive agents and protects it from being bleached[45]. Previous TPSM studies on single eGFP molecules in live sup-T1 and 293T cells reported a bleach rate of 52.7 ± 5.2 seconds for a high laser power of 130.8 mW[9]. Our results are consistent with these findings, as we illuminate eGFP molecules at very low laser intensities of 1.6 mW, thereby strongly reducing the chance of being excited to higher-order excited states. Rhodamine 6G molecules do not feature a protective barrel to shield them from radical agents, and indeed we see much faster bleaching. Importantly, the rhodamine molecules were imaged in air and hence no stabilizing agents nor oxygen scavengers were present in their surroundings. For *in vivo* measurements we did not observe photobleaching of eGFP and would recommend its use for TPM studies.

In one-photon microscopy, it has been shown that SIM can cause artefacts when the images are reconstructed from low contrast data[46]. Therefore SIM is commonly used for imaging larger assemblies and more densely packed fluorophores instead of single fluorophores[47,48]. Indeed, we found that for imaging larger and brighter structures such as blood vessels in zebrafish embryos, SLIM offers excellent reduction in background compared to spiral illumination and we did not observe artefacts.

SLIM diminishes the result of scattering of emission photons in wide-field detection without additional hardware. Due to the two-photon non-linear excitation mechanism, which yields a sharper excitation PSF, super resolution reconstruction could further improve image resolution compared to conventional SIM. This would require multiple orientation angles of the illumination pattern but would enhance the effects of read noise[49]. Future studies will need to experimentally find the optimal settings for TPMM SLIM super resolution.

In this work we focused on tracking single molecules with different TPMM modes. The disparity in number of observed fluorophores *in vitro* between spiral illumination and SLIM is likely caused by two factors. First, the increase in camera readout noise impaired fluorophore visibility. Second, incomplete spatial sampling of the image plane will result in missed fluorophores. Although hardly visible in single frames, the SLIM illumination pattern is distinguishable in the maximum intensity projection of the brain of a zebrafish embryo (Figure S4.2). Note that the width of excitation PSF is narrower than the emission PSF, so the observed gaps in the two-photon fluorescence underestimate the gaps in the illumination pattern[37]. For imaging larger cellular structures a low-pass image filtering may suffice to remove such illumination artefacts[50]. However, for imaging individual fluorophores the focal plane should be sampled with a finer mesh. No illumination artifacts were observed in the spiral illumination projection, which indicates that spiral illumination samples the image plane more homogeneously. Spatial under-sampling would also explain the higher signal intensity of SLIM for single molecules as the excitation power is distributed over a smaller area. Increasing the number of phase-images would result in higher homogeneity but also increases the read noise. Six-phase images per reconstruction proved to be the best compromise between SNR and spatial sampling.

SLIM+ reduced the degenerative effect of readout noise and sampled the focal plane more homogeneously by combining three lines per phase image. This allowed us to image single eGFP-HRas proteins without noticeable modulations in signal. However, this was difficult to assess in the fluorescently sparse samples.

When excitation power is inhomogeneously distributed across the focal plane, trace trajectories could be interrupted which would impair the tracking of a particle. The MSD from the SLIM+ measurement was lower than that of the spiral illumination, which could be an indication of spatial modulation in excitation power. Please note that biological variations between cells could also explain the difference in MSD. Another degenerative signal modulation during SLIM acquisition could arise when a particle moves fast enough to skip an illumination line between phase images and will not be detected after reconstruction. When a particle moves along the illumination lines, its signal would also be filtered out by the Fourier transformation. The broader excitation lines in SLIM+ acquisition reduces effects of a particle movement as only three phase-images are required and the faster frame rate may also be advantageous. Despite the higher SNR of SLIM+, the abovementioned concerns suggest that spiral illumination provides the most robust method for tracking of single molecules, as was also indicated by 3D tracking of gold nanorods in live cells[34].

We measured a disparity in confinement and diffusion constant between the different traces between spiral illumination, SLIM+ and TIRF. More extensive research by TIRF microscopy on HRas proteins in live 3T3-A14 cells showed that the dynamics of HRas could be modelled to a fast, freely diffusing state and a confined state within a 0.2 μm^2 domain[51]. Likely, averaging all traces by a MSD curve is insufficient to differentiate the states of a single HRas protein from the long trajectories TPMM produces. Assessing the traces individually, or using more specific automated analysis models should further validate the potential of TPMM for single molecule tracking studies.

A different microscopy technique which combines fast acquisition speeds and low photobleaching is two photon light-sheet microscopy. Due to the lower excitation NA however, there might be concern whether two-photon light-sheet microscopy can generate enough fluorescent signal for single molecule detection. Considering a spherically focused beam, the probability for two-photon excitation in the focal volume scales with NA^4 (equation 4.5) while the volume itself scales with NA^{-4} as explained in[37]. This means that the total amount of fluorescence from the focal volume is independent on NA. Thus, a lower signal intensity per voxel is compensated with exciting a larger number of voxels. Indeed, imaging with the same resolution and average excitation power, the total signal acquisition rates of two-photon light-sheet and single-point scanning microscopy are similar to each other[52]. To match the higher count rate per voxel of a point-focused microscope, the dwell time of the excitation beam has to be increased to collect the same amount of signal. According to this logic, two-photon light-sheet microscopy should be able to image single fluorophores at similar SNR as TPSM[9,14,15], and does not perform as well as TPMM in terms of frame rate.

To increase acquisition rate by a factor N, the laser beam of TPLM would need $\sqrt{N}$ more excitation power, owing to the squared signal dependence on power. In comparison, an increase in acquisition rate with TPMM goes linear with the number of foci. So the same N times increase in frame rate is accompanied with N number of foci and N times more average excitation power. A higher average laser power increases one photon absorption and photodamage which impedes long time-lapse studies. However, the major advantage of light-sheet microscopy comes from the reduced peak intensities. Peak intensity scales with NA^2 and the excitation NA of a light-sheet microscope is typically 4-10 times lower than TPMM or TPSM [52–55].

Lower peak intensities translate to longer bleaching times. It has been suggested that bleaching times increase as a result of a lower contribution of higher order (2>) absorption events[52,56]. This would be a significant advantage to extend single molecule time traces. Alternatively, reduced photo-damage makes higher average laser powers possible, which should enable TPLM to reach faster acquisition speeds or higher SNR compared to TPMM. TPLM has also been combined with structured illumination to reduce scattered emission photons[57]. The light-sheet thickness will however be inherently thicker in TPLM due to the lower illumination NA which would impair spatial resolution. Still, the lower phototoxicity or higher SNR suggest that TPLM is a competitive alternative to TPMM for wide-field single molecule imaging, though to the best of our knowledge, single molecule imaging has not been reported using TPLM.

In conclusion, we demonstrated *in vivo* two-photon fluorescence of single molecules by wide-field detection. Our results indicate that low excitation power distributed over multiple foci results in lower bleach rates compared to single point scanning and very limited bleaching of eGFP molecules *in vivo*. Unwanted scattering of emitted light in *in vivo* imaging applications were reduced to below single-molecule levels using SLIM and SLIM+. Besides single molecule sensitivity, lower bleach rates and higher frame rates allowed for long time-lapse studies on single eGFP-HRas fluorophores in live zebrafish embryos. This is the first time that two-photon single molecule tracking in wide field has been reported. We expect that the high quality and long time traces that can be obtained TPMM will expand the wide range of biophysical experiments and provide new insights in molecular dynamics in complex biological samples.

4.5 SUPPLEMENTARY FIGURES

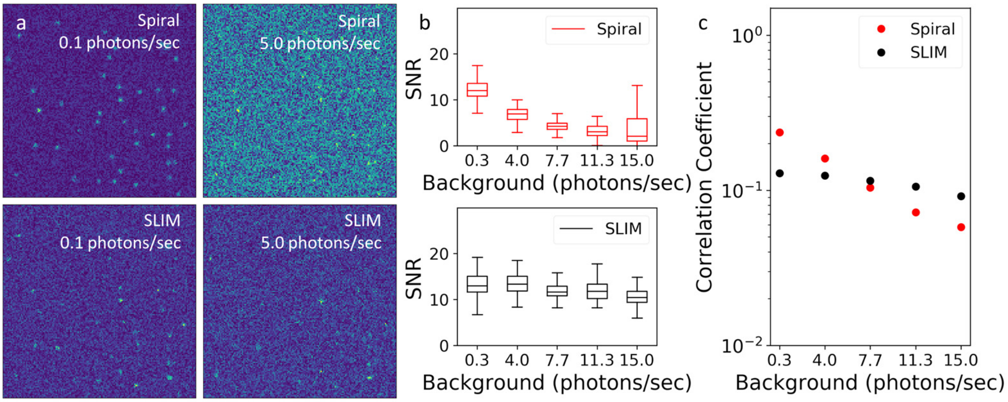

Figure S4.1: Simulations to investigate the influence on background noise for both spiral scanning and SLIM. (a) Four ROIs for both illumination modalities at low noise conditions and high noise conditions. At 0.1 e^-/sec, spiral scanning captures more fluorophores than SLIM. However, at 5.0 e^-/sec the background suppression of SLIM provides a higher fidelity. (b) The distribution of the SNR of 150 fluorophores for spiral and SLIM for a range of noise levels. SNR reduces in spiral imaging due to increased background while for SLIM it remains relatively stable. (c) The correlation coefficient in respect to the ground truth. Around 2.6 e^-/sec SLIM overtakes spiral scanning in how much the image resembles the ground truth image.

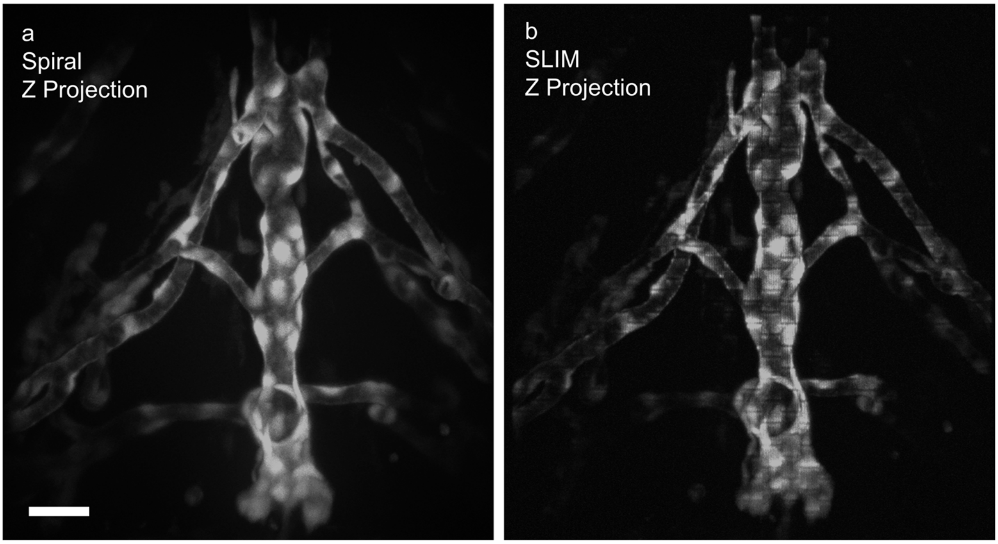

Figure S4.2. Rapid multifocal scanning combined with TPE allows for 3D imaging of blood vessels in the brain of zebrafish embryos. (a) Maximum intensity projection of a volume of 700 images taken over a depth of 350 µm from the brain of a zebrafish embryo via spiral scanning. mTurquoise fused to *kdrl* expressing endothelial cells mark the blood vessel walls. (b) Maximum z-projection of the same volume as in *a*, illuminated via SLIM. The projection features some SLIM illumination artefacts (e.g. a slightly inhomogeneous illumination). Scale bar = 25 µm.

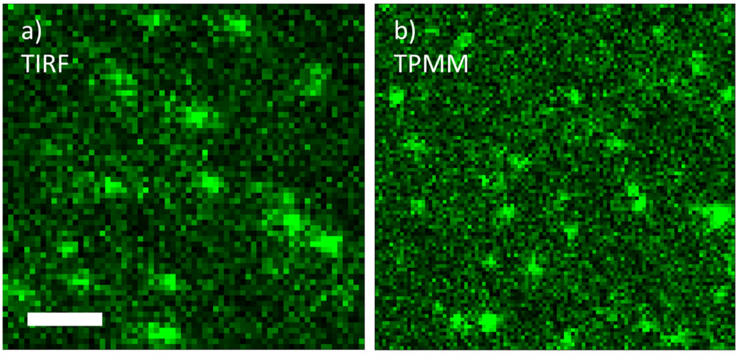

Figure S4.3: One-photon TIRF microscopy and TPMM/SLIM+ show very similar images when measuring eGFP labelled HRas proteins in live zebrafish embryos, indicating TPMM single molecule fluorescence. (a) A TIRF image of a region of a skin cell showing spots originating from single fluorescent proteins. Scale bar = 2 µm. (b) A TPMM/SLIM+ image of a different area of the same size, featuring similar diffraction limited spots.

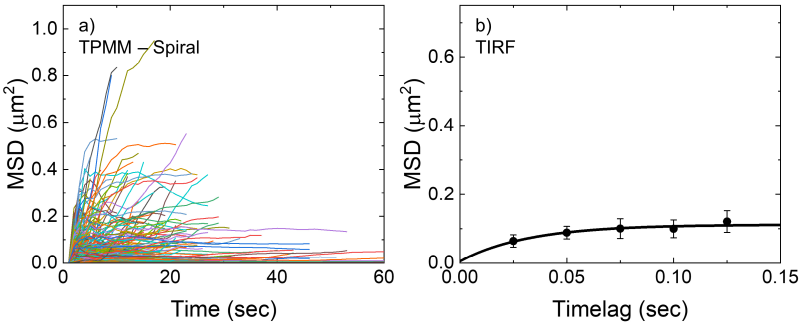

Figure S4.4: TPMM and TIRF microscopy feature different time-dependent MSD curves. (a) MSD curves of individual traces from a TPMM measurement using spiral illumination. Some traces last for tens of seconds. There is a large spread in confinement and diffusion coefficient between the molecules. (b) Typical MSD curve from a TIRF measurement on HRas molecules located in the interior membrane of the cell. The confinement of 0.33 ± 0.10 µm features a very small deviation from its mean. Note that this curve was generated using the PICS algorithm[58], which combines displacement of all peaks into a single MSD curve.

4.6 BIBLIOGRAPHY

1. Axelrod, D. Cell-substrate contacts illuminated by total internal reflection fluorescence. *J. Cell Biol.* **89**, 141–145 (1981).
2. Hohlbein, J. *et al.* Reports on Progress in Physics Related content Fluorescence correlation spectroscopy : the technique and its applications Fluorescence correlation spectroscopy : the technique. *Reports Prog. Phys.* **65**, 251–297 (2002).
3. Segers-Nolten, G. M. J. Scanning confocal fluorescence microscopy for single molecule analysis of nucleotide excision repair complexes. *Nucleic Acids Res.* **30**, 4720–4727 (2002).
4. Pierobon, P. *et al.* Velocity, processivity, and individual steps of single myosin V molecules in live cells. *Biophys. J.* **96**, 4268–4275 (2009).
5. Denk, W., Strickler, J. H. & Webb, W. W. Two-Photon Laser Scanning Fluorescence Microscopy. *Sci. New Ser.* **248**, 73–76 (1990).
6. Biermann, B. *et al.* Imaging of molecular surface dynamics in brain slices using single-particle tracking. *Nat. Commun.* (2014). doi:10.1038/ncomms4024
7. Berland, K. M., So, P. T. C. & Gratton, E. Two-Photon Fluorescepce Correlation Spectroscopy : Method and Application to the Intracellular Environment. *Biophys. J.* **68**, 694–701 (1995).
8. Farrer, R. A. *et al.* Single-molecule detection with a two-photon fluorescence microscope with fast-scanning capabilities and polarization sensitivity. *Opt. Lett.* **24**, 1832 (1999).
9. Hou, X. & Cheng, W. Detection of single fluorescent proteins inside eukaryotic cells using two-photon fluorescence. *Biomed. Opt. Express* **3**, 340 (2012).
10. Sanchez, E. J., Novotny, L., Holtom, G. R. & Xie, X. S. Room-Temperature Fluorescence Imaging and Spectroscopy of Single Molecules by Two-Photon Excitation. **101**, 0–4 (1997).
11. Hou, X. & Cheng, W. Single-molecule detection using continuous wave excitation of two-photon fluorescence. *Opt. Lett.* **36**, 3185 (2011).
12. Lewis, M. K., Wolanin, P., Gafni, A. & Steel, D. G. Near-field scanning optical microscopy of single molecules by femtosecond two-photon excitation. *Opt. Lett.* **23**, 1111 (1998).
13. Sonnleitner, M., Schütz, G. . & Schmidt, T. Imaging individual molecules by two-photon excitation. *Chem. Phys. Lett.* **300**, 221–226 (1999).
14. Chirico, G., Cannone, F., Baldini, G. & Diaspro, A. Two-Photon Thermal Bleaching of Single Fluorescent Molecules. *Biophys. J.* **84**, 588–598 (2003).
15. Chirico, G., Cannone, F., Beretta, S., Baldini, G. & Diaspro, A. Single molecule studies by means of the two-photon fluorescence distribution. *Microsc. Res. Tech.* **55**, 359–364 (2001).
16. Mertz, J., Xu, C. & Webb, W. W. Single-molecule detection by two-photon-excited fluorescence. *Opt. Lett.* **20**, 2532 (1995).
17. Chen, T.-S., Zeng, S.-Q., Luo, Q.-M., Zhang, Z.-H. & Zhou, W. High-Order Photobleaching of Green Fluorescent Protein inside Live Cells in Two-Photon Excitation Microscopy. *Biochem. Biophys. Res. Commun.* **291**, 1272–1275 (2002).
18. Eggeling, C., Volkmer, A. & Seidel, C. A. M. Molecular photobleaching kinetics of

Rhodamine 6G by one- and two-photon induced confocal fluorescence microscopy. *ChemPhysChem* **6**, 791–804 (2005).
19. Patterson, G. H. & Piston, D. W. Photobleaching in Two-Photon Excitation Microscopy. *Biophys. J.* **78**, 2159–2162 (2000).
20. Niu, F. *et al.* Photobleaching of ultrashort pulses with different repetition rates in two-photon excitation microscopy. *Laser Phys.* **29**, 046001 (2019).
21. Sanchez, E. J., Novotny, L., Holtom, G. R. & Xie, X. S. Room-temperature fluorescence imaging and spectroscopy of single molecules by two-photon excitation. *J. Phys. Chem. A* **101**, 7019–7023 (1997).
22. Straub, M. & Hell, S. W. Multifocal multiphoton microscopy : a fast and efficient tool for 3-D fluorescence imaging. *Bioimaging* **6**, 177–185 (1998).
23. Sacconi, L. *et al.* Multiphoton multifocal microscopy exploiting a diffractive optical element. *Opt. Lett.* **28**, 1918 (2003).
24. Quicke, P. *et al.* High speed functional imaging with source localized multifocal two-photon microscopy. *Biomed. Opt. Express* **9**, 3678 (2018).
25. Fittinghoff, D. N., Wiseman, P. W. & Squier, J. A. Widefield multiphoton and temporally decorrelated multifocal multiphoton microscopy. *Opt. Express* **7**, 273 (2000).
26. Nielsen, T., Fricke, M., Hellweg, D. & Andresen, P. High efficiency beam splitter for multifocal multiphoton microscopy. *J. Microsc.* **201**, 368–376 (2001).
27. Martini, J., Andresen, V. & Anselmetti, D. Scattering suppression and confocal detection in multifocal multiphoton microscopy. *J. Biomed. Opt.* **12**, 034010 (2007).
28. Kim, K. H. *et al.* Multifocal multiphoton microscopy based on multianode photomultiplier tubes. *Opt. Express* **15**, 11658 (2007).
29. Cha, J. W. *et al.* Non-descanned multifocal multiphoton microscopy with a multianode photomultiplier tube. *AIP Adv.* **5**, 084802 (2015).
30. Ingaramo, M. *et al.* Two-photon excitation improves multifocal structured illumination microscopy in thick scattering tissue. *Proc. Natl. Acad. Sci.* **111**, 5254–5259 (2014).
31. Isobe, K. *et al.* Enhancement of lateral resolution and optical sectioning capability of two-photon fluorescence microscopy by combining temporal-focusing with structured illumination. **4**, 10565–10573 (2013).
32. Urban, B. E. & Zhang, H. F. Imaging neuronal structure dynamics using 2-photon super-resolution patterned excitation reconstruction microscopy. 1–9 (2018). doi:10.1002/jbio.201700171
33. Saumya Saurabh, Suvrajit Maji & Marcel P. Bruchez. Evaluation of sCMOS cameras for detection and localization of single Cy5 molecules. *Opt. Soc. Am.* (2012).
34. Van den Broek, B., Oosterkamp, T. H. & van Noort, J. A Multifocal Two-Photon Microscopy Setup for Parallel 3D Tracking of Gold Nanorods. *Biophys. J.* **98**, 178a (2010).
35. Bussmann, J. & Schulte-Merker, S. -. *Unpublished* (2011).
36. Schaaf, M. J. M. *et al.* Single-Molecule Microscopy Reveals Membrane Microdomain Organization of Cells in a Living Vertebrate. *Biophys. J.* **97**, 1206–1214 (2009).
37. Zipfel, W. R., Williams, R. M. & Webb, W. W. Nonlinear magic: Multiphoton microscopy in the biosciences. *Nat. Biotechnol.* **21**, 1369–1377 (2003).
38. So, P. T. C., Dong, C. Y., Masters, B. R. & Berland, K. M. Two-Photon Excitation Fluorescence Microscopy. *Annu. Rev. Biomed. Eng.* 399–429 (2000).

39. Tinevez, J. Y. *et al.* TrackMate: An open and extensible platform for single-particle tracking. *Methods* **115**, 80–90 (2017).
40. Dittrich, P. S. & Schwille, P. Photobleaching and stabilization of fluorophores used for single-molecule analysis with one- and two-photon excitation. *Appl. Phys. B Lasers Opt.* **73**, 829–837 (2001).
41. Liu, X., Rudolph, W. & Thomas, J. L. Photobleaching resistance of stimulated parametric emission in microscopy. *Opt. Lett.* **34**, 304 (2009).
42. Marian, C. M., Etinski, M. & Rai-Constapel, V. Reverse intersystem crossing in rhodamines by near-infrared laser excitation. *J. Phys. Chem. A* **118**, 6985–6990 (2014).
43. Chen, T. S., Zeng, S. Q., Zhou, W. & Luo, Q. M. A Quantitative Theory Model of a Photobleaching Mechanism. *Chinese Phys. Lett.* **20**, 1940–1943 (2003).
44. Schwille, P., Haupts, U., Maiti, S. & Webb, W. W. Molecular dynamics in living cells observed by fluorescence correlation spectroscopy with one- and two-photon excitation. *Biophys. J.* **77**, 2251–2265 (1999).
45. Brejc, K. *et al.* Structural basis for dual excitation and photoisomerization of the Aequorea victoria green fluorescent protein. *Proc. Natl. Acad. Sci. U. S. A.* **94**, 2306–2311 (1997).
46. Wegel, E. *et al.* Imaging cellular structures in super-resolution with SIM, STED and Localisation Microscopy: A practical comparison. *Sci. Rep.* **6**, 1–13 (2016).
47. Biteen, J. & Willets, K. A. Introduction: Super-Resolution and Single-Molecule Imaging. *Chem. Rev.* **117**, 7241–7243 (2017).
48. Hirano, Y., Matsuda, A. & Hiraoka, Y. Recent advancements in structured-illumination microscopy toward live-cell imaging. *Microscopy* **64**, 237–249 (2015).
49. Gustafsson, M. G. L. Nonlinear structured-illumination microscopy: Wide-field fluorescence imaging with theoretically unlimited resolution. *Proc. Natl. Acad. Sci. U. S. A.* **102**, 13081–13086 (2005).
50. Winter, P. W. *et al.* Incoherent structured illumination improves optical sectioning and contrast in multiphoton super-resolution microscopy. **23**, 260–265 (2015).
51. Lommerse, P. H. M., Snaar-Jagalska, B. E., Spaink, H. P. & Schmidt, T. Single-molecule diffusion measurements of H-Ras at the plasma membrane of live cells reveal microdomain localization upon activation. *J. Cell Sci.* **118**, 1799–1809 (2005).
52. Truong, T. V, Supatto, W., Koos, D. S., Choi, J. M. & Fraser, S. E. Deep and fast live imaging with two-photon scanned light-sheet microscopy. *Nat. Methods 2011 89* **8**, 757 (2011).
53. Fahrbach, F. O., Gurchenkov, V., Alessandri, K., Nassoy, P. & Rohrbach, A. Light-sheet microscopy in thick media using scanned Bessel beams and two-photon fluorescence excitation. *Opt. Express* **21**, 13824 (2013).
54. Lavagnino, Z., Cella Zanacchi, F., Ronzitti, E. & Diaspro, A. Two-photon excitation selective plane illumination microscopy (2PE-SPIM) of highly scattering samples: characterization and application. *Opt. Express* **21**, 5998 (2013).
55. Olarte, O. E. *et al.* Image formation by linear and nonlinear digital scanned light-sheet fluorescence microscopy with Gaussian and Bessel beam profiles. *Biomed. Opt. Express* **3**, 1492–505 (2012).
56. Ji, N., Magee, J. C. & Betzig, E. High-speed, low-photodamage nonlinear imaging using passive pulse splitters. *Nat. Methods* **5**, 197–202 (2008).
57. Zhao, M. *et al.* Cellular imaging of deep organ using two-photon Bessel light-sheet

nonlinear structured illumination microscopy. *Biomed. Opt. Express* **5**, 1296 (2014).

58. Semrau, S., Schmidt, T. Particle image correlation spectroscopy (PICS): Retrieving nanometer-scale correlations from high-density single-molecule position data. *Biophysical Journal* **92**, 613-621 (2007)